

A phase-field method for two-phase fluid flow in arbitrary domains

Junxiang Yang, Junseok Kim*

Department of Mathematics, Korea University, Seoul 02841, Republic of Korea

ARTICLE INFO

Article history:

Received 22 May 2019

Received in revised form 24 August 2019

Accepted 7 October 2019

Available online 19 October 2019

Keywords:

Modified Navier–Stokes equation

Ternary Cahn–Hilliard system

Arbitrary domains

Projection method

ABSTRACT

We present a practical and efficient numerical method for two-phase flow simulations in arbitrary domains. A simple mathematical equation for the two-phase fluid in arbitrary domains is used. The proposed method is based on the ternary Cahn–Hilliard (CH) system coupled with the modified Navier–Stokes (NS) equation. A complex domain is expressed by the third phase in the ternary system. When we solve the ternary CH system, we only solve the equation for one phase with the fixed third phase. The second phase value is obtained from the local mass conservation. A no-slip condition was imposed for the velocity on the arbitrary domain boundaries. The proposed method uses an unconditionally gradient stable type scheme (Y. Li et al., 2016) for the convective CH equation and a projection method for the modified NS equation. Various numerical experiments, such as the droplet movement in a cavity flow, the Rayleigh–Taylor instability in a porous media, droplet passing through a triangle-shaped solid structure, and droplet movement in a circuitous channel, were performed to demonstrate that the proposed method can deal with the two-phase flow in arbitrary domains.

© 2019 Elsevier Ltd. All rights reserved.

1. Introduction

Multiphase flow simulation is an important branch of computational fluid dynamics (CFD). In nature, the Rayleigh–Taylor instability is a famous phenomenon of multiphase flow, which can be applied to many problems, such as the supernova explosion, inertial confinement fusion, and atmospheric physics, etc. Another famous phenomenon occurring in multiphase flow is the Kelvin–Helmholtz instability, which can cause the formation of billowing cloud. In industrial fields, the multiphase flow has wide applications in many problems. For example, the liquid–liquid jet can be applied in ink-jet printer, the Rayleigh instability can be used in the coating of conducting cables, the double emulsion formation can be applied in liquid drug delivery, etc. Comparing with the single phase flow, multiphase flow problems contain the topology change of interface and evolution of the fluid–fluid interface must be captured. In addition, the surface tension also plays an important role in capillary driven flows. Recently developed numerical methods for multiphase flow simulation are volume of fluid (VOF) method [1], immersed boundary method [2,3], level set method [4], front tracking method [5], lattice Boltzmann method [6–9], SPH method [10], and phase-field method [11–13]. The phase-field method is popular in CFD because the interfacial change can be easily achieved by solving the phase field equation. Jacqmin [14] used the phase-field model to calculate the two-phase fluid flow problems. Recently, Roudbari et al. [15] presented a new quasi-incompressible model and its energy stable scheme for phase-field fluid simulations. For more details about

* Corresponding author.

E-mail address: cfdkim@korea.ac.kr (J. Kim).

URL: <http://www.math.korea.ac.kr/~cfdkim> (J. Kim).

the phase-field models for multiphase fluid flows, please see the review papers [16,17] and references therein. Mitchell et al. [18] presented a 3D phase field lattice Boltzmann method which can efficiently simulate the flow with large density ratios. Aihara et al. [19] developed a new multiphase flow model using the conservative Allen–Cahn (AC) equation. Zu and He [20] combined the phase-field and lattice Boltzmann method to simulate the binary incompressible fluid flow. Ren et al. [21] applied the conservative AC model into the lattice Boltzmann method, which also worked well in the simulation of binary flow. Fakhari et al. [22] proposed an improved phase-field lattice Boltzmann model for simulating the fluid flow with high density ratio. Later, Abadi et al. [23] proposed a new phase-field lattice Boltzmann model to simulate the three-phase flow with mass conservation. Although the researchers above have conducted many numerical studies on multiphase flow by using phase-field method, their studies are limited to rectangular domains.

Many multiphase flow phenomena in science and engineering applications usually occur in complex domains, such as the liquid drug delivery in microfluid devices, oil–water mixture in sinuous channel, flow in porous medium, etc. To simulate the multiphase flow problems in a domain with arbitrary shape, many efficient and useful numerical approaches have been proposed. Lepilliez et al. [24] proposed an efficient numerical method for two-phase flow in irregular domains by using the level-set method. To treat the boundary between solid and fluid, this method used the previous work [25], where the authors proposed a novel discretization based on energy minimization to account for the solid–fluid coupling in single flow. The numerical results showed that their method could also deal with the contact line problems. Zolfaghari et al. [26] developed a combined front-tracking/immersed-boundary method for the movement and deformation of viscoelastic droplet passing through a narrow channel. In this work, the interface between solid and fluid was represented by a series of Lagrangian points, the immersed boundary method was used to impose the solid wall boundary condition, and the front-tracking method was applied to capture the interface between different fluid components. The results illustrated that the proposed method could robustly simulate the viscoelastic two-phase flow in a complex domain. Liu et al. [27] developed the diffuse interface model with an etching multiblock method for two-phase flow contacting solid. This method decomposed the complex domain into multiple blocks of rectangle or square shapes, for each block, some ghost cells were placed to impose no-slip boundary condition. Moreover, this method allowed an efficient parallel computation. The comparisons with other experiment data showed that the proposed method was accurate and efficient. Li et al. [28] applied the Cartesian grid method for the binary CH in irregular domains. In this work, the complex domain was included in a larger rectangular computational domain. They used a domain control function to define the complex domain and it possessed the value 1 in complex domain and value 0 in the rest regions. Finally, they extended this method to simulate the droplet movement in a wavy channel. Fakhari and Bolster [29] used the lattice Boltzmann method to study droplet impact problems within the framework of structured Cartesian grids.

In this paper, we propose a simple and efficient computational method for the two-phase flow in arbitrary domains by using a phase-field method, which is based on the CH equation in complex domain [30]. The classical ternary CH system is modified into a practical binary CH equation with a fixed phase. Let the third phase be the fixed phase, then the shape of arbitrary domain is defined by the third phase. The contact angle boundary condition can be easily imposed by using the surface free energy function. Moreover, the no-slip boundary condition for velocity in an arbitrary domain is achieved by using a correction step. Physically, the tangential and normal velocity components of fluid should be zero along the interface between fixed solid and fluid domains. The free-slip boundary condition can be implemented using normal vector on the boundary, however, in this work we focus the no-slip boundary condition for simplicity of exposition. We can simulate the two-phase flow in an arbitrary domain by solving the modified CH equation coupled with the NS equation. The projection method and an unconditionally stable scheme are used to solve the NS equation and the modified CH equation, respectively. Recently, efficient and accurate computational methods for the CH equation have been proposed by Yang et al. [31], Cai et al. [32], and Xu and Tang [33], which can be directly applied to our method without major modifications.

The paper is organized in the following manner. We introduce the governing equation and contact angle boundary condition in Section 2. In Section 3, we give the numerical solution for the modified CH system with a contact angle. The numerical experiments are performed in Section 4. We give the conclusion in Section 5.

2. Governing equations

2.1. Modified Navier–Stokes–Cahn–Hilliard system

First, we briefly review the ternary CH system in a domain $\Omega \subset \mathbb{R}^d$. Here, we consider the two-dimensional space (i.e., $d = 2$). We denote concentrations by $c_i(\mathbf{x}, t)$ for $i = 1, 2, 3$. By the conservation of mass, we have

$$c_1(\mathbf{x}, t) + c_2(\mathbf{x}, t) + c_3(\mathbf{x}, t) = 1. \quad (1)$$

The ternary CH system is given as

$$\frac{\partial c_i}{\partial t} = M \Delta \mu_i, \quad (2)$$

$$\mu_i = f(c_i) - \epsilon^2 \Delta c_i + \beta(c_1, c_2, c_3), \quad \text{for } i = 1, 2, 3. \quad (3)$$

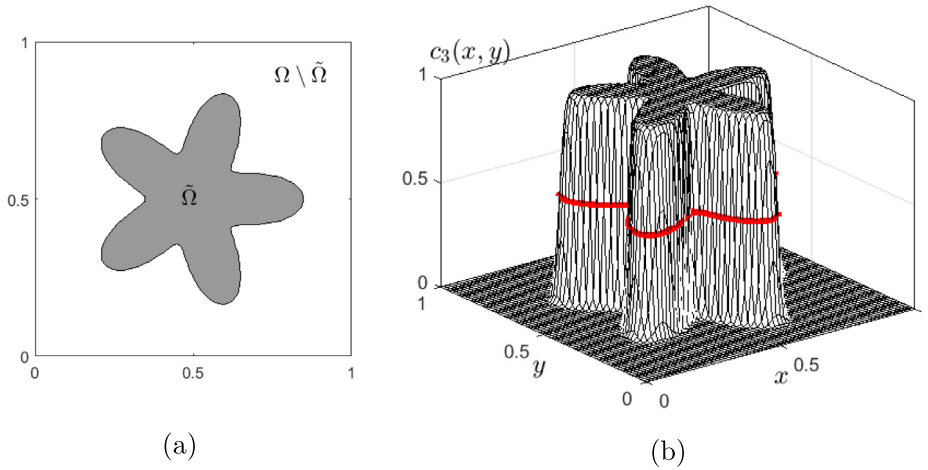


Fig. 1. (a) Ω embedding $\tilde{\Omega}$ and (b) $c_3(x, y)$.

Here, M is a constant mobility, $F(c_i) = 0.25c_i^2(1 - c_i)^2$ is a double well potential, $\epsilon > 0$, $f(c_i) = F'(c_i) = c_i(c_i - 0.5)(c_i - 1)$, and $\beta(c_1, c_2, c_3) = -\frac{1}{3} \sum_{i=1}^3 f(c_i) = -c_1c_2c_3$. More details about the Lagrangian multiplier $\beta(c_1, c_2, c_3)$ can be found in [34,35] and references therein. In the proposed method, c_3 is used to represent an arbitrary domain, $\tilde{\Omega} \subset \Omega$. That is, $c_3 \approx 1$ on $\tilde{\Omega}$ and $c_3 \approx 0$ on $\Omega \setminus \tilde{\Omega}$. As shown in Fig. 1, the 0.5-level set of c_3 is $\partial\tilde{\Omega}$. Recalling Eq. (1), we only need to compute c_1 over the computational domain because c_3 is fixed during the computation and $c_2 = 1 - c_1 - c_3$ can be straightforwardly obtained. Therefore, the modified CH model can be written as

$$\frac{\partial c_1}{\partial t} = M \Delta \mu_1, \tag{4}$$

$$\mu_1 = f(c_1) - \epsilon^2 \Delta c_1 - c_1c_2c_3. \tag{5}$$

For two-phase fluid flow, the modified NS equation is defined by

$$\rho(\mathbf{c})(\mathbf{u}_t + \mathbf{u} \cdot \nabla \mathbf{u}) = -\nabla p + \nabla \cdot [\eta(\mathbf{c})(\nabla \mathbf{u} + \nabla \mathbf{u}^T)] + \mathbf{SF}(\mathbf{c}) + \rho(\mathbf{c})\mathbf{g}, \tag{6}$$

$$\nabla \cdot \mathbf{u} = 0 \quad \text{on } \Omega, \tag{7}$$

where \mathbf{u} , p , $\rho(\mathbf{c}) = \rho_1c_1 + \rho_2c_2$, and $\eta(\mathbf{c}) = \eta_1c_1 + \eta_2c_2$ are the velocity, pressure, variable density, and viscosity, respectively. The densities of fluid 1 and 2 are represented by ρ_1 and ρ_2 , respectively. The viscosities of fluid 1 and 2 are represented by η_1 and η_2 , respectively. The gravitational force is \mathbf{g} . The surface tension is defined as [36]:

$$\mathbf{SF}(\mathbf{c}) = -6\sqrt{2}\epsilon \nabla \cdot \left(\frac{\nabla c_1}{|\nabla c_1|} \right) |\nabla c_1| \nabla c_1. \tag{8}$$

If we put all Eqs. (4)–(7) together and add the advection term to Eq. (4), then we have the following governing equations for two-phase flow in an arbitrary domain:

$$\rho(\mathbf{c})(\mathbf{u}_t + \mathbf{u} \cdot \nabla \mathbf{u}) = -\nabla p + \nabla \cdot [\hat{\eta}(\mathbf{c})(\nabla \mathbf{u} + \nabla \mathbf{u}^T)] + \mathbf{SF}(\mathbf{c}) + \rho(\mathbf{c})\mathbf{g}, \tag{9}$$

$$\nabla \cdot \mathbf{u} = 0, \tag{10}$$

$$\frac{\partial c_1}{\partial t} + \nabla \cdot (c_1 \mathbf{u}) = M \Delta \mu_1, \tag{11}$$

$$\mu_1 = f(c_1) - \epsilon^2 \Delta c_1 - c_1c_2c_3, \tag{12}$$

where we note that c_3 is fixed and represents an arbitrary domain. $\hat{\eta}(\mathbf{c}) = \eta_1c_1 + \eta_2c_2 + \eta_3c_3$ is the variable viscosity over the domain. Let η_3 be the viscosity of solid phase and $\eta_3 \gg \eta_1$, $\eta_3 \gg \eta_2$. After non-dimensionalization [37], the dimensionless form of Eqs. (9)–(12) can be written as

$$\rho(\mathbf{c})(\mathbf{u}_t + \mathbf{u} \cdot \nabla \mathbf{u}) = -\nabla p + \frac{1}{Re} \nabla \cdot [\hat{\eta}(\mathbf{c})(\nabla \mathbf{u} + \nabla \mathbf{u}^T)] + \frac{1}{We} \mathbf{SF}(\mathbf{c}) \tag{13}$$

$$+ \frac{\rho(\mathbf{c})}{Fr^2} \mathbf{g},$$

$$\nabla \cdot \mathbf{u} = 0, \tag{14}$$

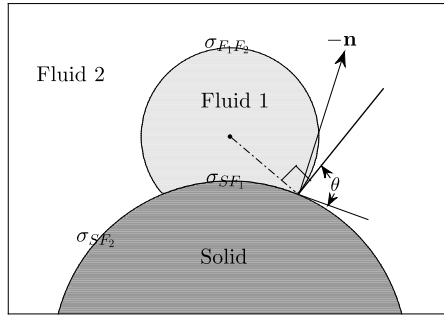


Fig. 2. Schematic illustration of contact angle between fluid and solid.

$$\frac{\partial c_1}{\partial t} + \nabla \cdot (c_1 \mathbf{u}) = \frac{1}{Pe} \Delta \mu_1, \tag{15}$$

$$\mu_1 = f(c_1) - \epsilon^2 \Delta c_1 - c_1 c_2 c_3. \tag{16}$$

The dimensionless numbers above are Reynolds number: $Re = \rho_c U_c L_c / \eta_c$, Weber number: $We = \rho_c L_c U_c^2 / \sigma$, Froud number: $Fr^2 = U_c^2 / (g L_c)$, and Peclet number: $Pe = U_c L_c / (M \mu_c)$, where $\rho_c, U_c, L_c, \eta_c, \mu_c$ are the characteristic density, velocity, length, viscosity, and chemical potential, respectively. σ and g are the surface tension coefficient and the gravitational acceleration, respectively.

2.2. Contact angle boundary condition

The contact angle between fluid and solid plays an important role in wetting or non-wetting simulations. In an equilibrium state, the contact angle θ follows the Young’s equation [38]

$$\sigma_{F_1 F_2} \cos \theta = \sigma_{SF_1} - \sigma_{SF_2}, \tag{17}$$

where $\sigma_{F_1 F_2}, \sigma_{SF_1}$, and σ_{SF_2} are the surface tension coefficients at the interfaces between fluid 1–fluid 2, solid–fluid 1, and solid–fluid 2. A schematic illustration is shown in Fig. 2.

In our scheme, the solid domain is defined by a fixed phase c_3 , therefore, the following condition is satisfied on the boundary of c_3

$$\nabla c_1 \cdot \mathbf{n} = -|\nabla c_1| \cos \theta, \tag{18}$$

where c_1 is a fluid phase, $\mathbf{n} = \nabla c_3 / |\nabla c_3|$ is a normal vector to the boundary of c_3 . From [39], we can get the relation: $|\nabla c_1| = c_1(1 - c_1) / (\sqrt{2}\epsilon)$. Hence, we can rewrite Eq. (18) as

$$\epsilon c_1(c_1 - 1) |\nabla c_3| \cos \theta / \sqrt{2} + \epsilon^2 \nabla c_3 \cdot \nabla c_1 = 0. \tag{19}$$

We put Eq. (19) into Eq. (16) and consider the constraint condition in Eq. (1), then the modified CH model with a contact angle boundary condition can be written as the following form

$$\frac{\partial c_1}{\partial t} + \nabla \cdot (c_1 \mathbf{u}) = \frac{1}{Pe} \nabla \cdot [(1 - c_3) \nabla \mu_1], \tag{20}$$

$$\begin{aligned} \mu_1 = & f(c_1) - c_1 c_2 c_3 + \frac{\epsilon c_1(c_1 - 1) |\nabla c_3| \cos \theta}{\sqrt{2}} \\ & - \epsilon^2 \nabla \cdot ((1 - c_3) \nabla c_1). \end{aligned} \tag{21}$$

3. Numerical solution

We first describe the numerical procedure for the modified CH model with a contact angle boundary condition. The full computational domain is specified as $\Omega = (a, b) \times (c, d)$. We define the discrete domain $\Omega^h = \{(x_i, y_j) | 1 \leq i \leq N_x, 1 \leq j \leq N_y\}$, where $x_i = a + (i - 0.5)h, y_j = c + (j - 0.5)h$. N_x and N_y are the numbers of mesh grid and the uniform mesh size $h = (b - a) / N_x = (d - c) / N_y$. The time step is defined as $\Delta t = T / N_t$, where T is the final computational time, N_t is the number of time steps. Let $c_{1,ij}^n$ and d_{ij} be the approximations of $c_1(x_i, y_j, n\Delta t)$ and $1 - c_3(x_i, y_j)$, respectively. An unconditionally gradient stable scheme [40] is used to discretize Eqs. (20) and (21) as the following form

$$\frac{c_{1,ij}^{n+1} - c_{1,ij}^n}{\Delta t} = M \nabla_d \cdot (d_{ij} \nabla_d \mu_{1,ij}^{n+1}) - \nabla_d \cdot (c_1 \mathbf{u})_{ij}^n, \tag{22}$$

$$\begin{aligned} \mu_{1,ij}^{n+1} &= f(c_{1,ij}^{n+1}) + 0.25c_{1,ij}^{n+1} - 0.25c_{1,ij}^n - \epsilon^2 \nabla_d \cdot (d_{ij} \nabla_d c_{1,ij}^{n+1}) \\ &\quad - c_{1,ij}^n c_{2,ij}^n c_{3,ij} + \frac{\epsilon c_{1,ij}^n (c_{1,ij}^n - 1) |\nabla_d c_{3,ij}| \cos \theta}{\sqrt{2}}. \end{aligned} \tag{23}$$

The discrete Laplacian operators $\nabla_d \cdot (d_{ij} \nabla_d \mu_{1,ij}^{n+1})$ and $\nabla_d \cdot (d_{ij} \nabla_d c_{1,ij}^{n+1})$ take the following form

$$\begin{aligned} \nabla_d \cdot (d_{ij} \nabla_d \phi_{1,ij}^{n+1}) &= \frac{d_{i+1/2,j}(\phi_{1,i+1,j}^{n+1} - \phi_{1,ij}^{n+1}) - d_{i-1/2,j}(\phi_{1,ij}^{n+1} - \phi_{1,i-1,j}^{n+1})}{h^2} \\ &\quad + \frac{d_{i,j+1/2}(\phi_{1,i,j+1}^{n+1} - \phi_{1,ij}^{n+1}) - d_{i,j-1/2}(\phi_{1,ij}^{n+1} - \phi_{1,i,j-1}^{n+1})}{h^2}, \end{aligned}$$

where $d_{i+1/2,j} = (d_{i+1,j} + d_{ij})/2$. The value of $|\nabla_d c_{3,ij}|$ is computed by the central difference scheme

$$|\nabla_d c_{3,ij}| = \sqrt{\left(\frac{c_{3,i+1,j} - c_{3,i-1,j}}{2h}\right)^2 + \left(\frac{c_{3,i,j+1} - c_{3,i,j-1}}{2h}\right)^2}. \tag{24}$$

Eqs. (22) and (23) are solved by a nonlinear multigrid method [41], please see [42] for more detailed information of multigrid method. For mass conservation, the following conservative discretization of advection term in Eq. (22) is used

$$\begin{aligned} \nabla_d \cdot (c_1 \mathbf{u})_{ij}^n &= \frac{\mathbf{u}_{i+1/2,j}^n (c_{1,i+1,j}^n + c_{1,ij}^n) - \mathbf{u}_{i-1/2,j}^n (c_{1,ij}^n + c_{1,i-1,j}^n)}{2h} \\ &\quad + \frac{\mathbf{v}_{i,j+1/2}^n (c_{1,i,j+1}^n + c_{1,ij}^n) - \mathbf{v}_{i,j-1/2}^n (c_{1,ij}^n + c_{1,i,j-1}^n)}{2h}. \end{aligned} \tag{25}$$

As for the NS equation in an arbitrary domain, it is solved by using the projection method [43] with a correction step. The main procedures for solving Eqs. (13)–(14) are as follows:

Step 1. Give the initial values c_1^0 , c_3 , and \mathbf{u}^0 which satisfies the divergence-free condition.

Step 2. Compute the intermediate velocity field $\tilde{\mathbf{u}}$ without pressure gradient.

$$\rho(\mathbf{c})^n \frac{\tilde{\mathbf{u}} - \mathbf{u}^n}{\Delta t} = \frac{1}{Re} \nabla_d \cdot [\hat{\eta}(\mathbf{c})^n (\nabla_d \mathbf{u} + \nabla_d \mathbf{u}^T)^n] \tag{26}$$

$$+ \frac{1}{We} \mathbf{SF}(\mathbf{c}^n) + \frac{\rho(\mathbf{c})^n}{Fr^2} \mathbf{g} - \rho(\mathbf{c})^n (\mathbf{u}^n \cdot \nabla_d \mathbf{u}^n). \tag{27}$$

Step 3. Compute the pressure by solving the following Poisson equation with a linear multigrid method [17,41].

$$\nabla_d \cdot \left(\frac{1}{\rho(\mathbf{c})^n} \nabla_d p^{n+1} \right) = \frac{1}{\Delta t} \nabla_d \cdot \tilde{\mathbf{u}}^n. \tag{28}$$

Step 4. Compute the velocity field which satisfies the divergence-free condition.

$$\mathbf{u}^{n+1} = \tilde{\mathbf{u}} - \frac{\Delta t}{\rho(\mathbf{c}^n)} \nabla_d p^{n+1}. \tag{29}$$

Step 5 (Correction step). Update the velocity field by correcting \mathbf{u}^{n+1} in fluid or solid domain.

$$\mathbf{u}^{n+1} = \lambda \mathbf{u}^{n+1}, \tag{30}$$

where λ is domain indicating parameter, we set $\lambda = 1$ in fluid domain and $\lambda = 0$ in solid domain. In the phase-field method, the 0.5-level set is used to represent the interface between solid and fluid and the λ is defined as

$$\lambda = \begin{cases} 0 & \text{if } c_3 > 0.5, \\ 1 - 2c_3 & \text{otherwise,} \end{cases}$$

which means the velocity decreases to 0 along the half of transition region. We note that this approach treats the half of transition region to be a boundary layer if we use a small enough transition width. Steps 1–5 complete the computation of the NS equation in one time step, please see [17] for the detailed numerical scheme of the NS equation.

Now, we describe the discretizations of the boundary conditions for velocity \mathbf{u} in the following tests: cavity flow, Rayleigh–Taylor instability, droplet passing through obstacle, and droplet in channel. In this work, a staggered marker-and-cell (MAC) mesh [44] is used, where the pressure p and phase-field variable \mathbf{c} are stored at cell centers and velocities u and v are stored at cell edges. A schematic illustration of MAC mesh can be found in Fig. 3. In solid domains, the no-slip type boundary condition is used for u and v by using the correction step in Eq. (30).

For the cavity flow in Section 4.3, we use the no-slip boundary condition and $u = 1$ at the top boundary:

$$\begin{aligned} u_{\frac{1}{2},j} &= 0, \quad u_{N_x+\frac{1}{2},j} = 0, \\ v_{0,j} &= -v_{1,j}, \quad v_{N_x+1,j} = -v_{N_x,j} \quad \text{for } j = 1, \dots, N_y, \end{aligned}$$

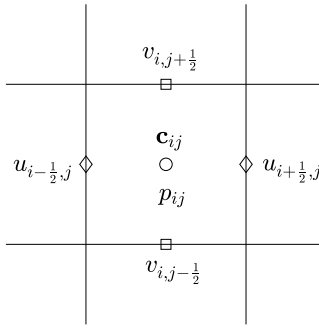


Fig. 3. Schematic illustration of marker-and-cell (MAC) mesh.

$$u_{i,0} = -u_{i,1}, \quad u_{i,N_y+1} = 2 - u_{i,N_y},$$

$$v_{i,1/2} = 0, \quad v_{i,N_y+1/2} = 0 \quad \text{for } i = 1, \dots, N_x.$$

For the Rayleigh–Taylor instability in Section 4.4, we use the periodic boundary condition along x -direction and no-slip boundary condition along y -direction:

$$u_{-1/2,j} = u_{N_x-1/2,j}, \quad u_{N_x+3/2,j} = u_{3/2,j},$$

$$v_{0,j} = v_{N_x,j}, \quad v_{N_x+1,j} = v_{1,j} \quad \text{for } j = 1, \dots, N_y,$$

$$u_{i,0} = -u_{i,1}, \quad u_{i,N_y+1} = -u_{i,N_y},$$

$$v_{i,-1/2} = -v_{i,3/2}, \quad v_{i,N_y+3/2} = -v_{i,N_y-1/2} \quad \text{for } i = 1, \dots, N_x.$$

For the droplet passing through obstacle and droplet in channel in Sections 4.6 and 4.8, we use the inflow and outflow boundary conditions along x -direction, the no-slip boundary condition is used along y -direction:

$$u_{1/2,j} = \hat{U}(y_j - \alpha)(\beta - y_j), \quad u_{N_x+3/2,j} = u_{N_x+1/2,j},$$

$$v_{0,j} = -v_{1,j}, \quad v_{N_x+1,j} = -v_{N_x,j} \quad \text{for } j = 1, \dots, N_y,$$

$$u_{i,0} = -u_{i,1}, \quad u_{i,N_y+1} = -u_{i,N_y},$$

$$v_{i,1/2} = 0, \quad v_{i,N_y+1/2} = 0 \quad \text{for } i = 1, \dots, N_x,$$

where \hat{U} is a constant coefficient, α and β represent the lower and upper boundary positions of inlet.

4. Numerical results

For simplicity, unless otherwise specified, the density and viscosity ratios are $\rho_1 : \rho_2 = 1 : 1$, $\eta_1 : \eta_2 : \eta_3 = 1 : 1 : 100$, where ρ_1 and ρ_2 are the densities of fluid 1 and fluid 2, η_1 , η_2 , and η_3 are the viscosities of fluid 1, fluid 2, and solid. For ϵ , we use the notion: $\epsilon_m = \frac{mh}{4\sqrt{2} \tanh^{-1}(0.9)}$, which implies that the number of grid points across the interface is approximately m [45].

4.1. Effect of mesh size

In this paper, the arbitrary solid domain is defined by the initial value of the third phase. To investigate the effect of mesh size on the artificial layer, we compute the CH system without flow on $\Omega = (0, 1) \times (0, 1)$. We use $\Delta t = 0.001$, $Pe = 1$, $\epsilon = \epsilon_4$, and contact angle $\theta = 90^\circ$. The initial conditions are

$$c_3(x, y) = 0.5 + 0.5 \tanh \left(\frac{0.3 - \sqrt{(x - 0.5)^2 + (y)^2}}{\sqrt{2}\epsilon} \right), \tag{31}$$

$$c_1(x, y, 0) = 0.5 + 0.5 \tanh \left(\frac{0.3 - \sqrt{(x - 0.5)^2 + (y - 0.3)^2}}{\sqrt{2}\epsilon} \right) - c_3(x, y), \tag{32}$$

$$c_2(x, y, 0) = 1 - c_1(x, y, 0) - c_3(x, y), \tag{33}$$

where c_3 represents the solid domain. The computation stops when the numerical solutions reach the equilibrium state, (i.e., $\|c_1^{n+1} - c_1^n\|_2 \leq 10^{-6}$). Fig. 4 illustrates a local view of interface profiles for different mesh sizes at equilibrium state. As we can see, the overlapped region is becoming smaller and local mass loss is decreasing as we refine the mesh size.

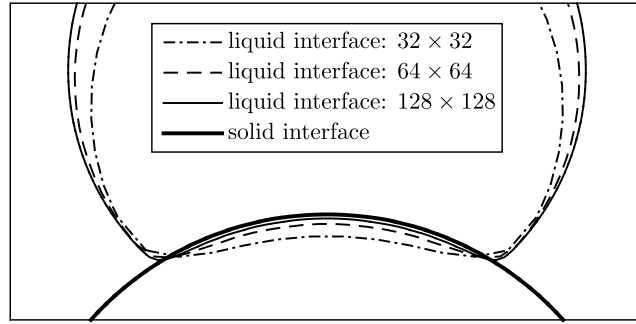


Fig. 4. A local view of interface profiles for different mesh sizes, 32×32 (dot dashed line), 64×64 (dashed line), 128×128 (solid line), at equilibrium state.

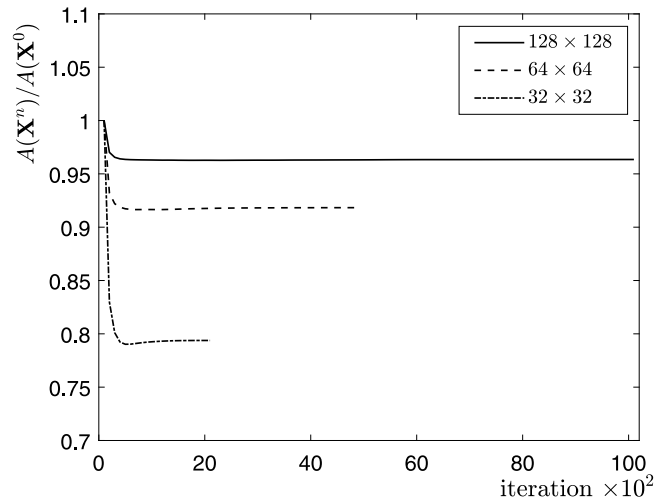


Fig. 5. Evolutions of normalized polygonal area with respect to different mesh sizes.

Table 1
Local mass loss with respect to different mesh sizes.

Mesh size	$A(\mathbf{X}^0)/A(\mathbf{X}^0)$	$A(\mathbf{X}^e)/A(\mathbf{X}^0)$	Error
32×32	1	0.7938	0.2062
64×64	1	0.9183	0.0817
128×128	1	0.9635	0.0365

To quantitatively show the local mass loss with respect to different mesh sizes, we define the polygonal area enclosing by the interface [46] as:

$$A(\mathbf{X}) = \frac{1}{2} \sum_m^M (X_m Y_{m+1} - Y_m X_{m+1}), \tag{34}$$

where \mathbf{X} represents the positions of points at interface, M represents the total numbers of points at interface. The evolutions of normalized polygonal area $A(\mathbf{X}^n)/A(\mathbf{X}^0)$ are shown in Fig. 5, where the superscripts n and 0 indicate the n th iteration and initial state, respectively. Note that we use $A(\mathbf{X}^e)$ to represent the polygonal area at equilibrium state. Table 1 illustrates the mass loss of area enclosed by interface with respect to different mesh sizes: 32×32 , 64×64 , and 128×128 . The error is defined as $Error = |1 - A(\mathbf{X}^e)/A(\mathbf{X}^0)|$. With the increase of mesh size, the local mass loss is decreasing.

4.2. Stability of the proposed scheme

In this work, we use the unconditionally stable scheme [40] to treat the CH equation without the convection term. For the CH equation without the convection term, this scheme satisfies the unconditionally energy stability. For the convective

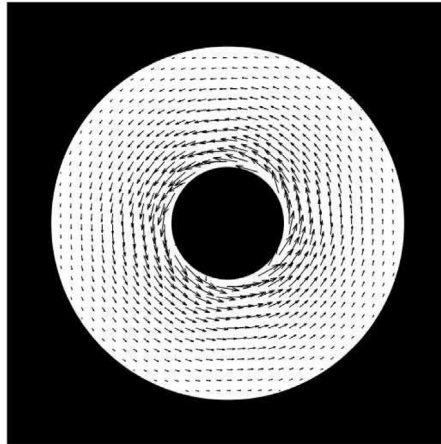


Fig. 6. Background Taylor–Couette flow.

CH system, it is not strictly unconditionally stable for any large time steps. However, the following numerical results show that larger time steps can still work well. To test our scheme for the convective CH equation, we consider the trapped spinodal decomposition occurring in a background Taylor–Couette flow. The whole domain is $(0, 2) \times (0, 2)$ and the computational domain is trapped by a smaller cylinder with radius 0.25 and a larger cylinder with radius 0.8. The background velocity field is

$$u(x, y) = \left(\frac{0.0676}{(x - 1)^2 + (y - 1)^2} - 0.0734 \right) (1 - y), \tag{35}$$

$$v(x, y) = \left(\frac{0.0676}{(x - 1)^2 + (y - 1)^2} - 0.0734 \right) (x - 1). \tag{36}$$

Fig. 6 shows the background flow in a Taylor–Couette cell, where c_3 is defined in the black regions. The initial condition for c_1 is $c_1(x, y, 0) = 0.5 + 0.1\text{rand}(x, y)$, where $\text{rand}(x, y)$ represents the random numbers between -1 and 1 . The numerical parameters are $h = 1/128$, $Pe = 0.1/\epsilon$, and $\epsilon = \epsilon_4$. Fig. 7 shows the temporal evolutions of the spinodal decomposition in a background Taylor–Couette flow with different time steps: $\Delta t = 0.1h^2$, h^2 , $10h^2$, and $100h^2$. We can numerically confirm the stability of the scheme with the advection term.

4.3. Droplet movement and deformation in a driven cavity flow

We simulate the droplet movement and deformation driven by cavity flow to compare the results in an embedded domain and a fully rectangular domain. The sizes of the embedded domain and rectangular domain are the same. In this test, gravity is ignored and density- and viscosity-matched conditions are considered. The embedded domain $\tilde{\Omega} = (0.5, 1.5) \times (0.5, 1.5) \times (0.5, 1.5)$ is embedded in the whole computational domain $\Omega_1 = (0, 2) \times (0, 2) \times (0, 2)$. The parameters $h = 1/128$, $\Delta t = 10h^2$, $Re = 50$, $We = 50$, $\epsilon = \epsilon_4$, and $Pe = 1/\epsilon$ are used. The magnitude of top wall velocity is 1. The initial conditions in the embedded domain are

$$c_3(x, y) = 0.5 + 0.5 \tanh \left(\frac{\max(|x - 1| - 0.5, |y - 1.5| - 0.5)}{\sqrt{2}\epsilon} \right), \tag{37}$$

$$c_1(x, y, 0) = 0.5 + 0.5 \tanh \left(\frac{0.2 - \sqrt{(x - 1.2)^2 + (y - 1.7)^2}}{\sqrt{2}\epsilon} \right), \tag{38}$$

$$c_2(x, y, 0) = 1 - c_1(x, y, 0) - c_3(x, y). \tag{39}$$

The same parameters are also used in the fully rectangular domain $\Omega_2 = (0, 1) \times (0, 1)$. Here, the initial droplet with radius 0.2 is located on $(0.7, 0.7)$. For the whole computational domain Ω_1 , the no-slip boundary condition for velocities is set on all solid regions. For the rectangular domain Ω_2 , the no-slip boundary condition is set on all boundaries. Fig. 8(a), (b), and (c) show the temporal evolutions of droplet movement in the whole computational domain, the embedded domain, and the fully rectangular domain, respectively. As we can see, the droplet shows very similar movement and deformation in those domains.

Fig. 9(a) and (b) illustrate the temporal evolutions of the normalized x -coordinate (X) and y -coordinate (Y) of the center of mass of the droplet. We can find that the evolutions of coordinate positions are also similar for an embedded domain and a rectangular domain.

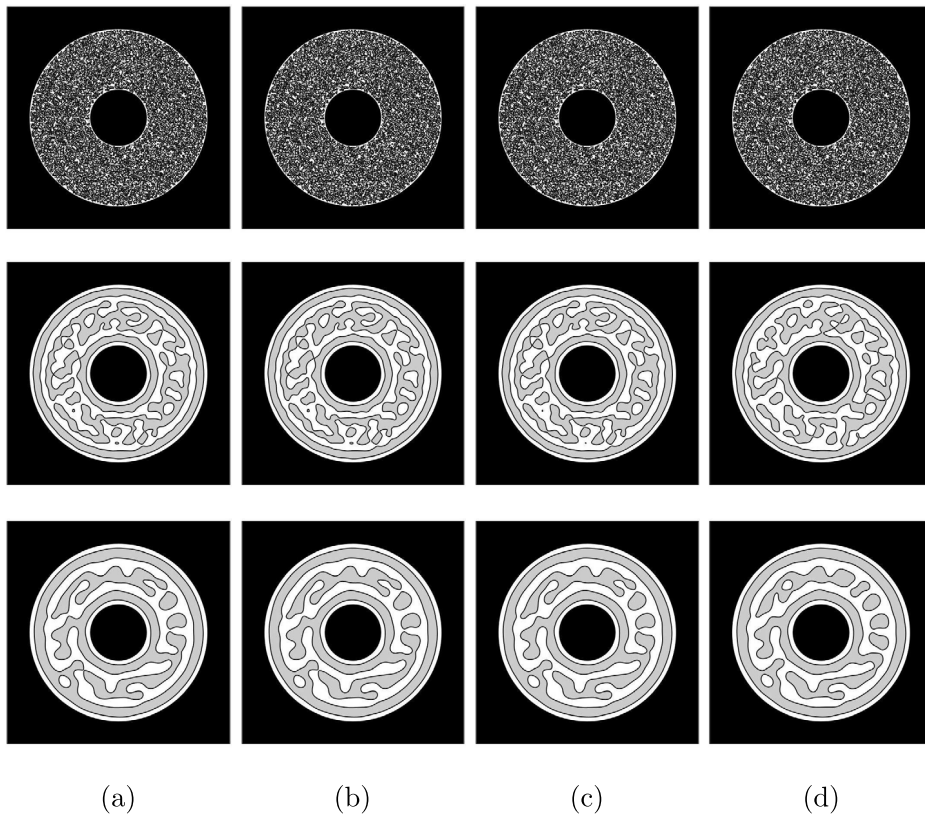


Fig. 7. Temporal evolutions of spinodal decomposition occurring in a Taylor–Couette flow with different time steps: (a) $\Delta t = 0.1h^2$, (b) $\Delta t = h^2$, (c) $\Delta t = 10h^2$, (d) $\Delta t = 100h^2$. The computational times from the top to bottom in each column are: $t = 0, 0.0916, 0.5493$.

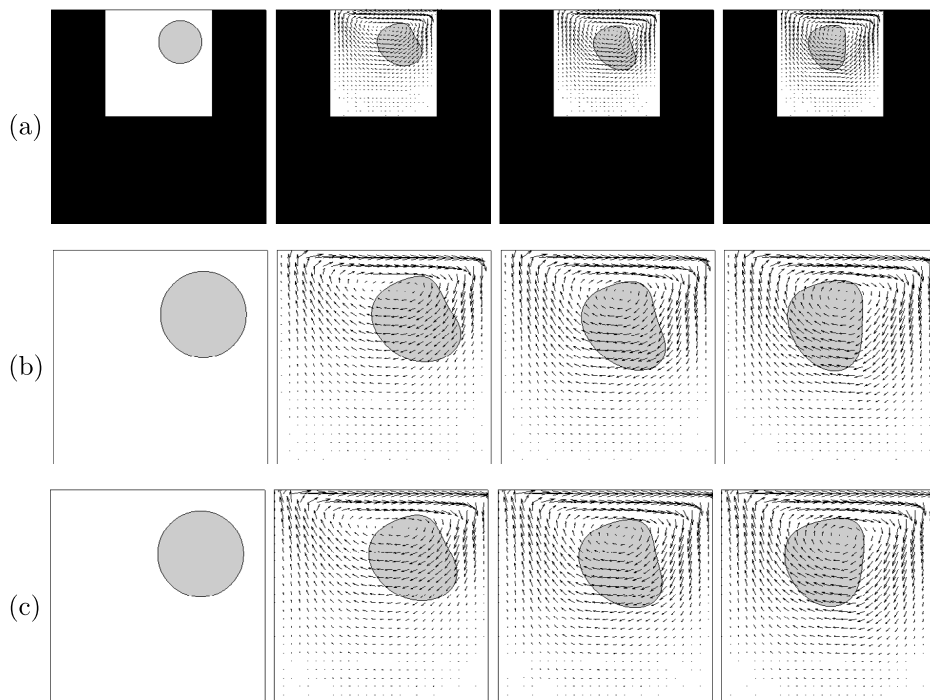


Fig. 8. Temporal evolutions of droplet movement in a driven cavity flow for (a) a whole computational domain, (b) an embedded domain, and (c) a fully rectangular domain. The times from left to right in each row are: $t = 0, 0.5493, 1.0986, 1.8311$.

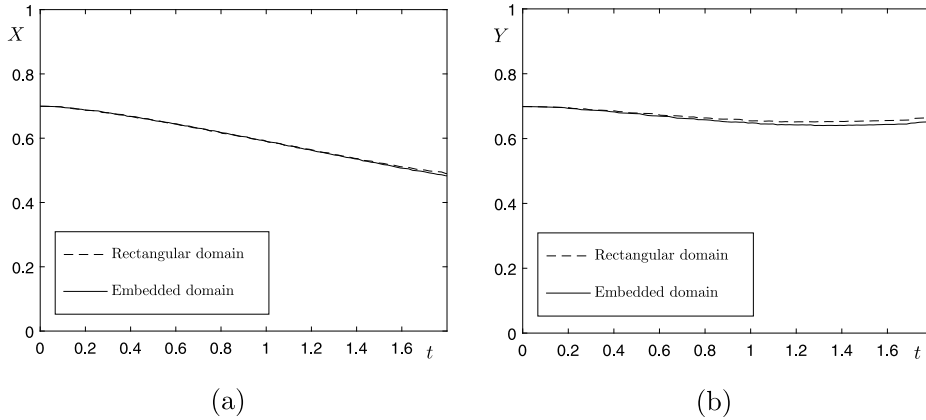


Fig. 9. Temporal evolutions of the normalized (a) x -coordinate (X) and (b) y -coordinate (Y) of the center of mass of the droplet for an embedded domain (dashed line) and a rectangular domain (solid line).

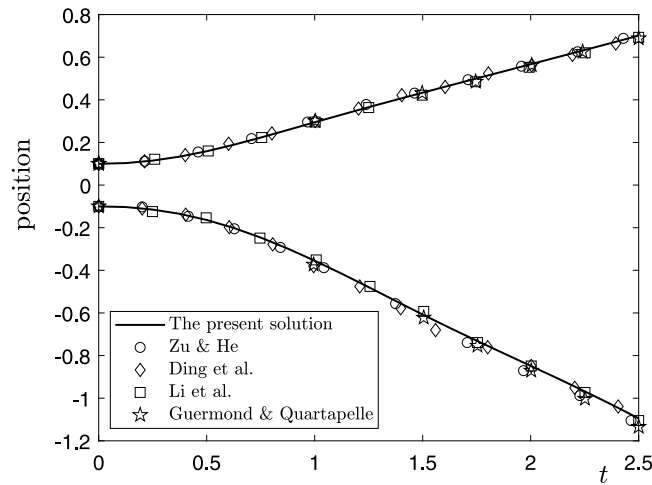


Fig. 10. Temporal evolutions of the rising and falling fluids. The solid line is the present solution, the open circle, open diamond, open square, and open star represent the results of Zu and He [20], Ding et al. [47], Li et al. [48], and Guermond and Quartapelle [49], respectively.

4.4. Rayleigh–Taylor instability in a porous medium

The Rayleigh–Taylor instability is mainly driven by the density difference, therefore we ignore the effect of surface tension (i.e., $We = \infty$) in this simulation. We first verify the solution of a single Rayleigh–Taylor instability by comparison with previous works performed by Zu and He [20], Ding et al. [47], Li et al. [48], and Guermond and Quartapelle [49]. The initial condition is defined as

$$c(x, y, 0) = 0.5 + 0.5 \tanh\left(\frac{y - 2 - 0.1 \cos(2\pi x)}{\sqrt{2}\epsilon}\right) \tag{40}$$

on the domain $\Omega = (0, 1) \times (0, 4)$. We use $h = 1/128$, $\Delta t = 0.0025$, $\epsilon = 0.01$, $Pe = 1/\epsilon$, $Re = 3000$, $At = (\rho_1 - \rho_2)/(\rho_1 + \rho_2) = 0.5$, and $Fr = 1$. The computation is performed until $t = 2.5$, which is related to ours by the time scale: $t = t\sqrt{At}$. The temporal evolutions of the rising and falling fluids are shown in Fig. 10. The numerical results show that our solution and the results of the previous works are in good agreement.

Then, we investigate the gravity-driven Rayleigh–Taylor instability with random initial condition in a porous medium. The porous region is defined by c_3 and we set the no-slip condition for velocities on the porous region. The initial conditions for c_1 and c_2 are given as

$$c_1(x, y, 0) = (1 - c_3(x, y)) \left(0.5 + 0.5 \tanh\left(\frac{y - 2 + 0.01\text{rand}}{\sqrt{2}\epsilon}\right)\right), \tag{41}$$

$$c_2(x, y, 0) = 1 - c_1(x, y, 0) - c_3(x, y), \tag{42}$$

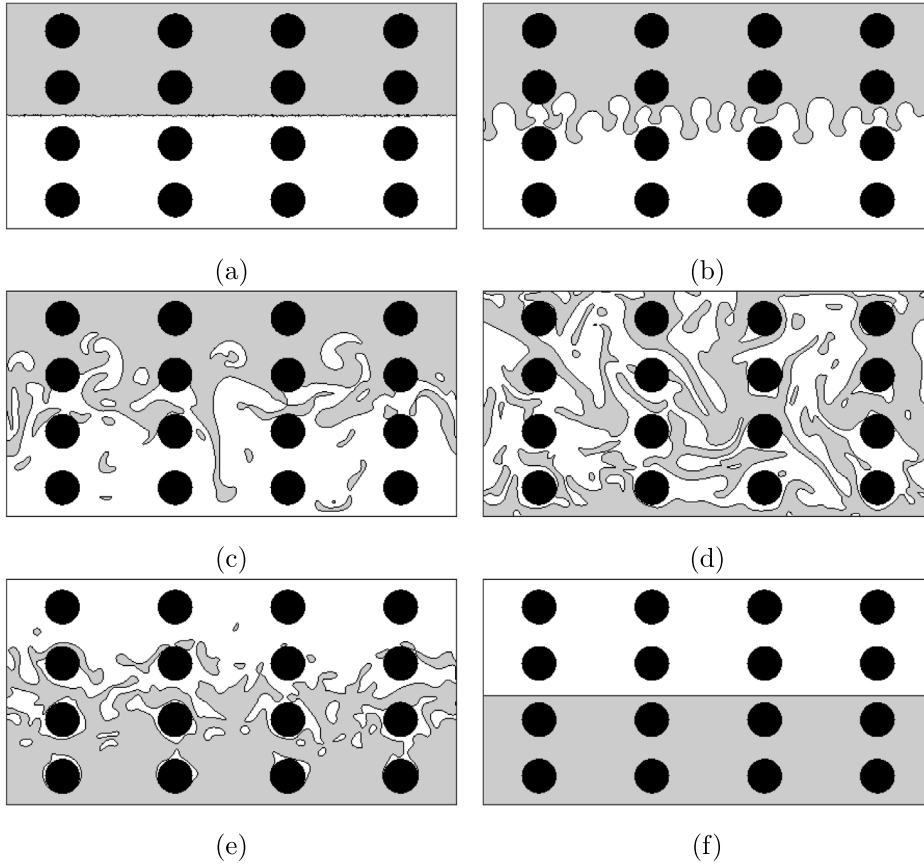


Fig. 11. Temporal evolution of Rayleigh–Taylor instability in a porous medium. The times from (a) to (f) are: $t = 0, 3.125, 9.375, 15.625, 28.125,$ and 312.5 .

$$u(x, y, 0) = v(x, y, 0) = 0 \tag{43}$$

on the whole computational domain $\Omega = (0, 4) \times (0, 2)$. Here, rand represents a random number between -1 and 1 . The upper heavier fluid is defined by c_1 and the lower lighter fluid is defined by c_2 . The other parameters are $h = 1/128, \Delta t = 0.2h, Re = 100, Fr = 1, \epsilon = \epsilon_4,$ and $Pe = 1/\epsilon$. The density ratio is $\rho_1 : \rho_2 = 3 : 1$. Fig. 11(a)–(f) illustrate the temporal evolution of Rayleigh–Taylor instability in a porous medium. In this porous medium, we can find that the initial perturbation on the interface grows as time proceeds, the heavier fluid flows down into the lighter fluid and results in the mixing. Finally, the heavier fluid completely goes down and the lighter fluid is on top of the heavier one.

Then, we further investigate the effect of initial wave number on the growth of minimum spike position and maximum bubble position in a porous medium. We chose one, two, and four initial wave numbers which are defined by Eqs. (44), (45), and (46), respectively.

$$c_1(x, y, 0) = (1 - c_3(x, y)) \left(0.5 + 0.5 \tanh \left(\frac{y - 2 - 0.03 \cos(0.5\pi x)}{\sqrt{2}\epsilon} \right) \right), \tag{44}$$

$$c_1(x, y, 0) = (1 - c_3(x, y)) \left(0.5 + 0.5 \tanh \left(\frac{y - 2 - 0.03 \cos(\pi x)}{\sqrt{2}\epsilon} \right) \right), \tag{45}$$

$$c_1(x, y, 0) = (1 - c_3(x, y)) \left(0.5 + 0.5 \tanh \left(\frac{y - 2 - 0.03 \cos(2\pi x)}{\sqrt{2}\epsilon} \right) \right), \tag{46}$$

where c_3 represents the porous medium. The computations are performed until $t = 2.5$. We show the snapshots at $t = 0$ and $t = 2.5$ in Fig. 12. The temporal growths of minimum spike position and maximum bubble position with different initial wave numbers are shown in Fig. 13. As we can see, although the porous medium suppresses the free evolution of the Rayleigh–Taylor instability, with the increase of initial wave number, the growth dynamics of spike and bubble is becoming faster.

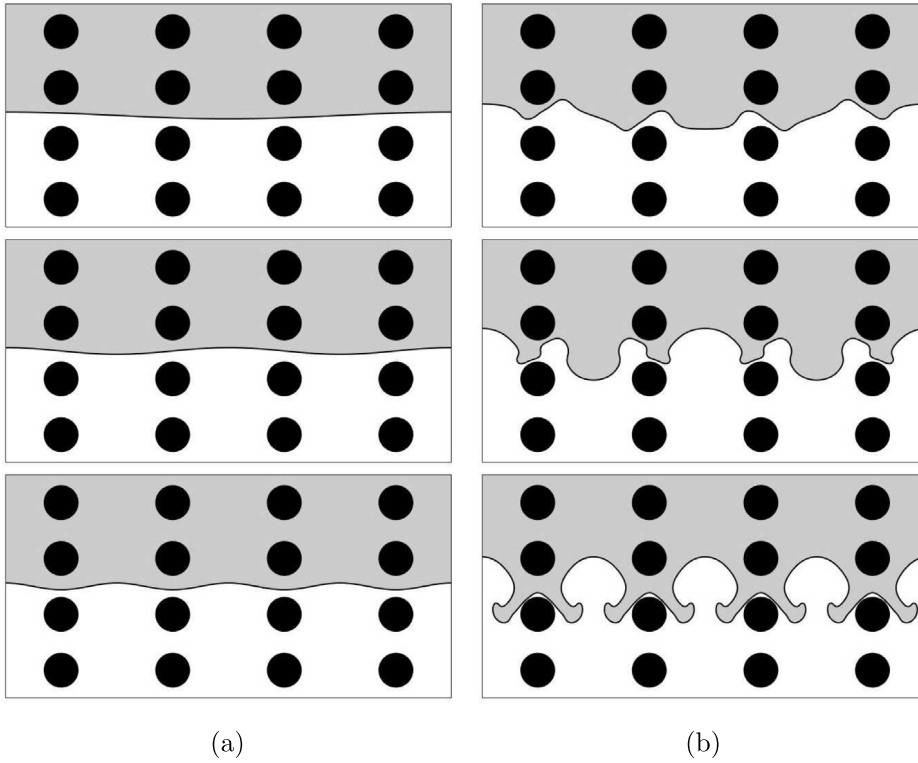


Fig. 12. Rayleigh–Taylor instability with different initial wave numbers in a porous medium: (a) $t = 0$ and (b) $t = 2.5$.

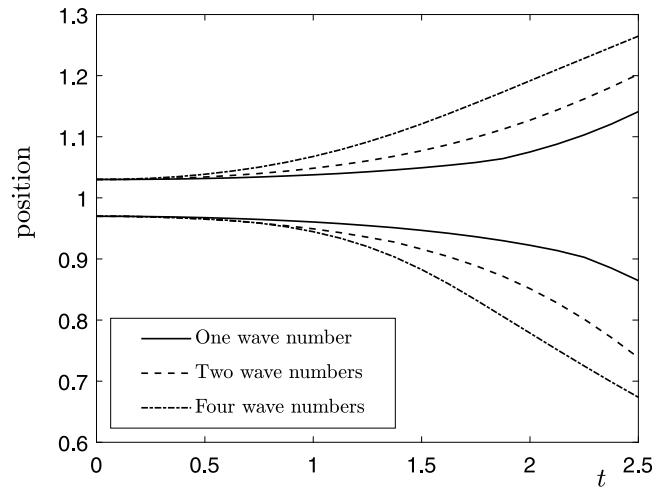


Fig. 13. Temporal growths of minimum spike position and maximum bubble position with different initial wave numbers.

4.5. Effect of contact angle without fluid flow

To study the effect of contact angle between the solid and droplet, we use $\theta = 30^\circ$ and $\theta = 150^\circ$ which represent the wetting and non-wetting conditions, respectively. We first investigate the equilibrium contact angle between the solid and liquid. The equilibrium state is determined as $\|c_1^{n+1} - c_1^n\|_2 \leq 10^{-6}$. Here, we solve the CH equation with $h = 1/128$, $\Delta t = 0.001$, $\epsilon = \epsilon_4$, $Pe = 1$ on the domain $\Omega = (1.5, 3.5) \times (0, 1)$. The initial conditions are given as

$$c_3(x, y) = 0.5 + 0.5 \tanh \left(\frac{-\max(|x - 2.25|) - 0.75, |y - 0.5| - (x/6 - 0.25)}{\sqrt{2}\epsilon} \right), \tag{47}$$

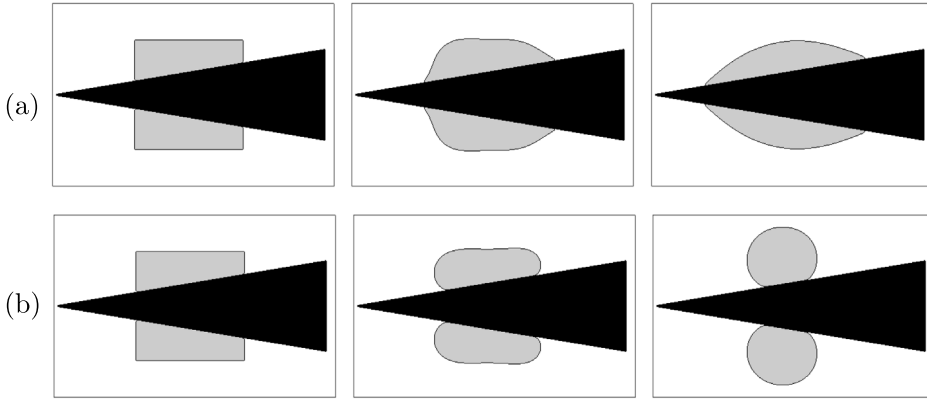


Fig. 14. Temporal evolutions with respect to different contact angles: (a) $\theta = 30^\circ$ and (b) $\theta = 150^\circ$. The times from left to right in each row are: $t = 0, 1, 20$ (equilibrium state).

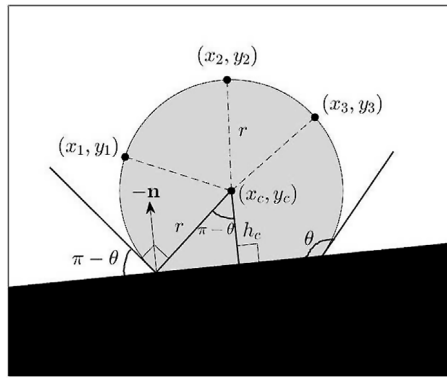


Fig. 15. Schematics illustration of the computation of numerical contact angle.

Table 2
Comparison between the numerical and exact contact angles.

Exact	30°	150°
Numerical	30.5351°	148.5937°

$$c_1(x, y, 0) = 0.5 + 0.5 \tanh \left(\frac{-\max(|x - 2.25| - 0.3, |y - 0.5| - 0.3)}{\sqrt{2}\epsilon} \right), \tag{48}$$

$$c_2(x, y, 0) = 1 - c_1(x, y, 0) - c_3(x, y). \tag{49}$$

Fig. 14(a) and (b) illustrate the temporal evolutions for $\theta = 30^\circ$ and $\theta = 150^\circ$, respectively. The solid phase is defined by c_3 (black) and the liquid phase is defined by c_1 (gray). We can find that an initial phase evolves to a specific shape with respect to θ .

To verify the proposed contact angle model, we compare the numerical contact angles with the exact values: 30° and 150° . To compute the numerical contact angle, we first choose three points: (x_1, y_1) , (x_2, y_2) and (x_3, y_3) locating on the interface, then we compute the center location (x_c, y_c) by using the following formulas:

$$(x_1 - x_c)^2 + (y_1 - y_c)^2 = (x_2 - x_c)^2 + (y_2 - y_c)^2, \tag{50}$$

$$(x_2 - x_c)^2 + (y_2 - y_c)^2 = (x_3 - x_c)^2 + (y_3 - y_c)^2. \tag{51}$$

Because radius r and center distance h_c satisfy the relation: $h_c = r \cos(\pi - \theta)$, hence the numerical contact angle can be easily obtained by $\theta = \pi - \cos^{-1}(h_c/r)$. A schematic illustration is shown in Fig. 15. Table 2 lists the numerical contact angles at equilibrium state and the exact values, we can observe that our results show good agreement with exact values.

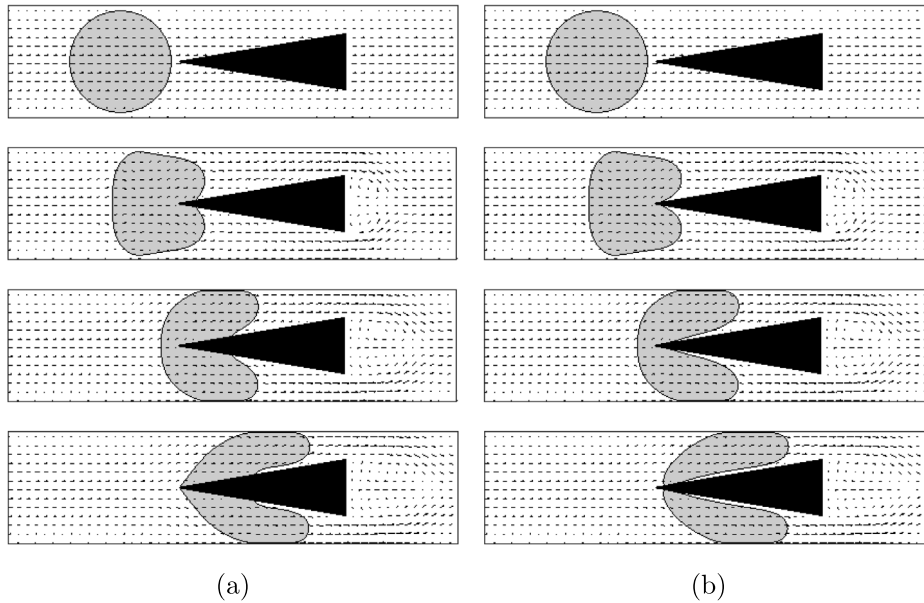


Fig. 16. Temporal evolutions of a droplet passing a triangle-shaped solid structure for (a) $\theta = 30^\circ$ and (b) $\theta = 150^\circ$. The times from the top to bottom in each column are: 0, 0.6104, 1.5259, 2.1362.

4.6. Effect of contact angle with fluid flow

Then, we further investigate the effect of contact angle with fluid flow. Here, parameters are $h = 1/128$, $\Delta t = 10h^2$, $Re = 100$, $We = 10$, $\epsilon = \epsilon_4$, $Pe = 0.1/\epsilon$. The effect of gravity is ignored. We set the inlet velocity as $u(0, y, t) = 3y(1 - y)$ on the left boundary of the whole computational domain $\Omega = (0, 4) \times (0, 1)$. To achieve a non-wetting condition on the top and bottom boundaries, the Dirichlet and no-slip boundary conditions are given for phase field variables and velocities, respectively. The initial conditions are given as

$$c_3(x, y) = 0.5 + 0.5 \tanh \left(\frac{-\max(|x - 2.25| - 0.75, |y - 0.5| - (x/6 - 0.25))}{\sqrt{2}\epsilon} \right), \tag{52}$$

$$c_1(x, y, 0) = 0.5 + 0.5 \tanh \left(\frac{0.45 - \sqrt{(x - 1)^2 + (y - 0.5)^2}}{\sqrt{2}\epsilon} \right), \tag{53}$$

$$c_2(x, y, 0) = 1 - c_1(x, y, 0) - c_3(x, y), \tag{54}$$

$$u(x, y, 0) = 1.0, \quad v(x, y, 0) = 0, \tag{55}$$

where triangle-shaped solid domain is defined by c_3 (black), the droplet is defined by c_1 (gray), and the continuum fluid phase is defined by c_2 (white), see Fig. 16. In this simulation, the no-slip condition for velocities is given on the solid domain. Fig. 16(a) and (b) show the temporal evolutions of a droplet passing a triangle-shaped solid structure for $\theta = 30^\circ$ and $\theta = 150^\circ$, respectively. Fig. 17(a) and (b) are the locally enlarged views of the bottom figures in Fig. 16(a) and (b). As we can see, the wetting and non-wetting processes can be found with $\theta = 30^\circ$ and $\theta = 150^\circ$, respectively.

4.7. Comparison with finite element simulation

The finite element method is an efficient and practical method for treating irregular domain. To investigate the practicability of our method, we consider the droplet drops along a rectangular hole. Chen et al. [50] used the binary Navier–Stokes–Allen–Cahn model to study this problem with different contact angles. The finite element discretization is used in their method to generate the irregular domain. In our test, the computational domain is $\Omega = (0, 2) \times (0, 2)$ which is similar with the size of domain in Chen et al. [50]. We use $\Delta t = 5h^2$, $h = 1/64$, $\rho_1 : \rho_2 = 6 : 1$, $Re = 1000$, and $Fr = 1$. The surface tension is absent in this simulation. Fig. 18(a) and (c) are the simulation results in Chen et al. [50] for different contact angles $\theta = 30^\circ$ and 150° , respectively; (b) and (d) are our simulation results at the corresponding times for different contact angles $\theta = 30^\circ$ and 150° . As we can see, our results are similar with those in the previous work performed by the finite element method.

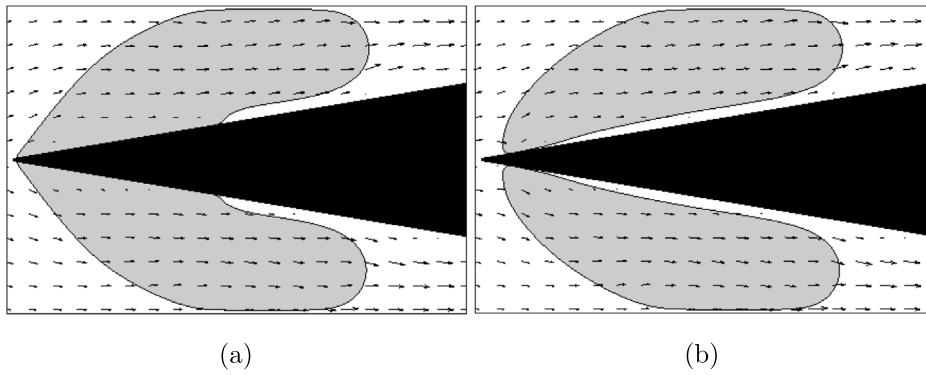


Fig. 17. The locally enlarged figures for (a) $\theta = 30^\circ$ and (b) $\theta = 150^\circ$ at $t = 2.1362$.

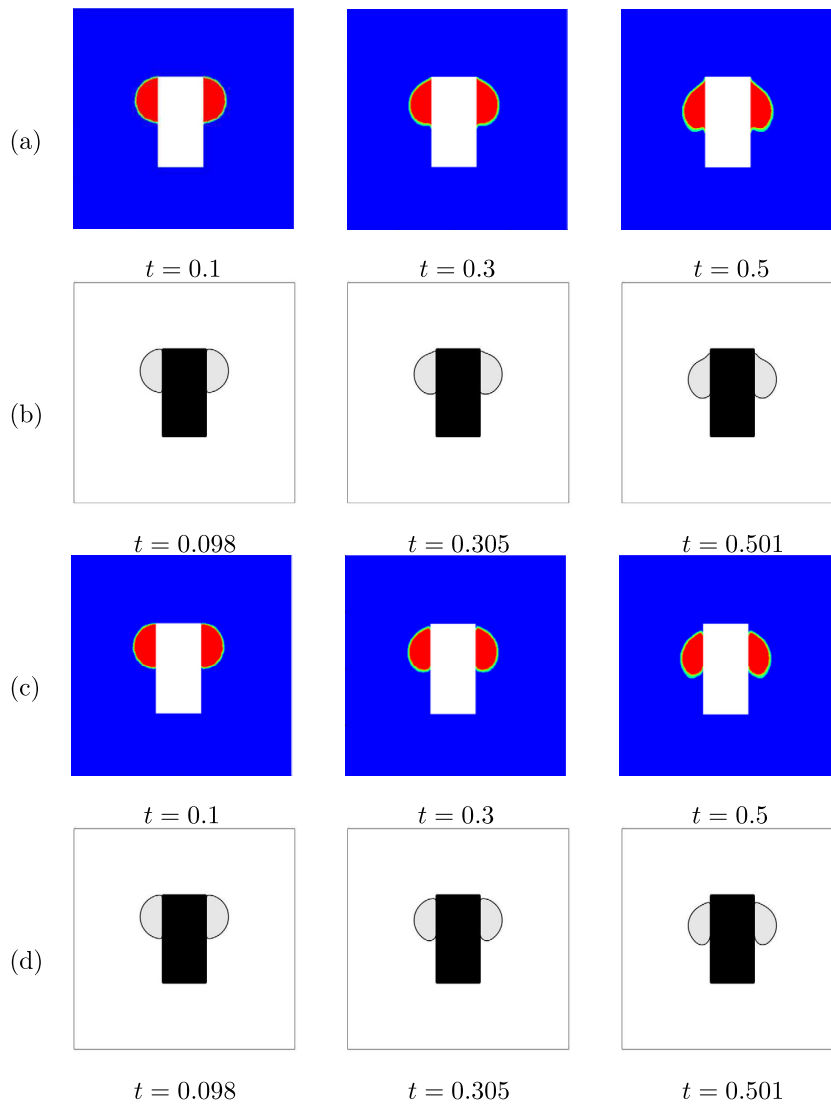


Fig. 18. Comparison with the finite element simulation. (a) and (c) are the simulation results with finite element method for different contact angles $\theta = 30^\circ$ and 150° , respectively. Adapted from Chen et al. [50] with the permission of Global Science Press. (b) and (d) are our simulation results for different contact angles $\theta = 30^\circ$ and 150° .

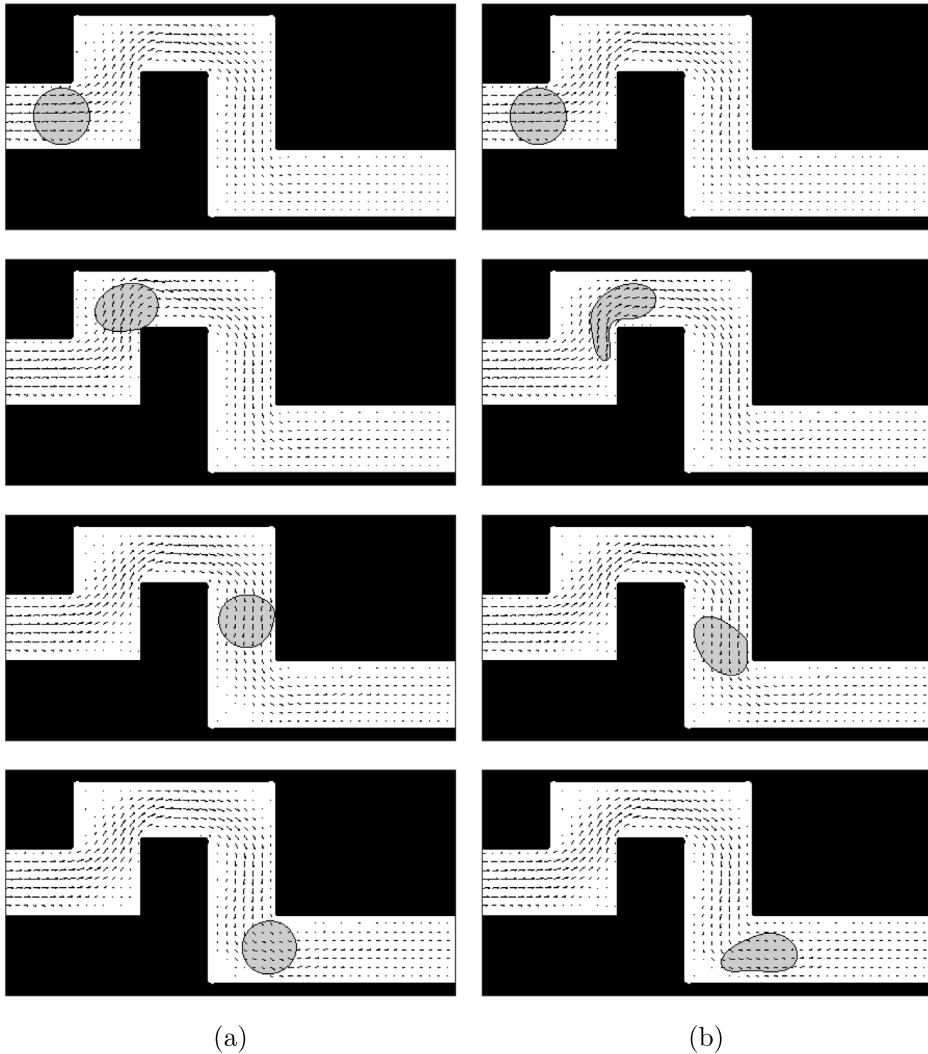


Fig. 19. Temporal evolution of a droplet movement in a circuitous channel for two different We : (a) 1 and (b) 10. The times from top to bottom in each column are: $t = 0, 0.0183, 0.0336, 0.0427$.

4.8. Effect of Weber number (We) on the droplet movement in a circuitous channel

Next, we study the movement of a droplet with different We in a circuitous channel. The solid region of channel is defined by the fixed shape of c_3 . The initial conditions for c_1 and c_2 are given as

$$c_1(x, y, 0) = 0.5 + 0.5 \tanh \left(\frac{0.28 - \sqrt{(x - 0.5)^2 + (y - 1)^2}}{\sqrt{2}\epsilon} \right), \tag{56}$$

$$c_2(x, y, 0) = 1 - c_1(x, y, 0) - c_3(x, y, 0) \tag{57}$$

on the whole domain $\Omega = (0, 4) \times (0, 2)$. The inlet velocity is $u(0, y, t) = 20(y - 0.7)(1.3 - y)$ for $0.7 \leq y \leq 1.3$ and the outlet boundary is given for $0.1 \leq y \leq 0.7$ on the right boundary. No-slip condition for velocities is given on the whole solid region. Other parameters are $h = 1/128, \Delta t = 10h^2, Re = 100, \epsilon = \epsilon_4,$ and $Pe = 1/\epsilon$. The effect of gravity is ignored. To achieve a non-wetting condition between the droplet and the solid wall, we use $\theta = 30^\circ$. Fig. 19(a) and (b) show the temporal evolution of a droplet in a circuitous channel for two different We : 1 and 10. As we can see, the droplet moves and deforms because of the effect of velocity fields and it does not contact with the solid wall since the non-wetting condition. A smaller We usually reflects a stronger effect of surface tension which suppresses the shape deformation in flow, therefore in Fig. 19(a), the deformation of droplet is smaller than that in Fig. 19(b).

5. Conclusion

We proposed a simple and efficient numerical method for the two-phase flow in arbitrary domains by using the phase field method. The ternary CH system was modified into a practical binary CH system with a fixed phase. The third phase is the fixed phase and the shape of arbitrary domain is defined by the initial value of the third phase. The contact angle boundary condition could be easily imposed by using the surface free energy function. We applied the unconditionally gradient stable scheme for the modified CH system and the multigrid method was used to solve the resulting system. For the NS equation, the projection method was used. Various numerical tests, such as the droplet movement in a cavity flow, Rayleigh–Taylor instability in a porous media, droplet passing through a triangle-shaped solid structure, and droplet movement in a circuitous channel, were performed to verify the practicability of the proposed method. The results demonstrate that our numerical method can practically deal with the two-phase flow problems in arbitrary domains.

Acknowledgment

The corresponding author (J.S. Kim) was supported by Basic Science Research Program through the National Research Foundation of Korea (NRF) funded by the Ministry of Education (NRF-2019R1A2C1003053).

References

- [1] H. Grosshans, A. Movaghar, L. Cao, M. Oevermann, R.Z. Szasz, L. Fuchs, Sensitivity of VOF simulations of the liquid jet breakup to physical and numerical parameters, *Comput. & Fluids* 136 (10) (2016) 312–323.
- [2] F. Nikfarjam, Y. Cheny, O. Botella, The LS-STAG immersed boundary/cut-cell method for non-Newtonian flows in 3D extruded geometries, *Comput. Phys. Comm.* 226 (2018) 67–80.
- [3] C.H. Yu, Tony W.H. Sheu, Development of a coupled level set and immersed boundary method for predicting dam break flows, *Comput. Phys. Comm.* 221 (2017) 1–18.
- [4] M.P. Kinzel, J.W. Lindau, R.F. Kunz, A multiphase level-set approach for all-Mach numbers, *Comput. & Fluids* 167 (15) (2018) 1–16.
- [5] M.R. Pivello, M.M. Villar, R. Serfaty, A.M. Roma, A. Silveira-Neto, A fully adaptive front tracking method for the simulation of two phase flows, *Int. J. Multiph. Flow.* 58 (2014) 72–82.
- [6] G. Di Ilio, D. Chiappini, S. Ubertini, G. Bella, S. Succi, A moving-grid approach for fluid–structure interaction problems with hybrid lattice Boltzmann method, *Comput. Phys. Comm.* 234 (2019) 137–145.
- [7] X. Yuan, Z. Chai, B. Shi, Dynamic behavior of droplet through a confining orifice: A lattice Boltzmann study, *Comput. Math. Appl.* 77 (2019) 2640–2658.
- [8] M.E.A.B. Amara, P. Perre, S.B. Nasrallah, Lattice–Boltzmann analysis of capillary rise, *J. Porous Media* 19 (5) (2016) 453–469.
- [9] P. Raiskinmäki, A. Shakib-Manesh, A. Jäsberg, A. Koponen, J. Merikoski, J. Timonen, Lattice–Boltzmann simulation of capillary rise dynamics, *J. Stat. Phys.* 107 (1) (2002) 143–158.
- [10] L. Chiron, M. de Lefle, G. Oger, D. le Touze, Fast and accurate SPH modelling of 3D complex wall boundaries in viscous and non viscous flows, *Comput. Phys. Comm.* 234 (2019) 93–111.
- [11] F. Li, X. Hu, A phase-field method for shape optimization of incompressible flows, *Comput. Math. Appl.* 77 (4) (2019) 1029–1041.
- [12] J. Yang, J. Kim, Phase-field simulation of Rayleigh instability on a fibre, *Int. J. Multiph. Flow.* 105 (2018) 84–90.
- [13] G. Zhu, J. Kou, S. Sun, J. Yao, A. Li, Decoupled, energy stable schemes for a phase-field surfactant model, *Comput. Phys. Comm.* 233 (2018) 67–77.
- [14] D. Jacqmin, Calculation of two-phase Navier–Stokes flows using phase-field modeling, *J. Comput. Phys.* 155 (1999) 96–127.
- [15] M.S. Roudbari, G. Simsek, E.H. van Brummelen, K.G. van der Zee, Diffuse-interface two-phase flow models with different densities: A new quasi-incompressible form and a linear energy-stable method, *Math. Models Methods Appl. Sci.* 28 (2018) 733–770.
- [16] Anderson, McFadden, Wheeler, Diffuse-interface models in fluid mechanics, *Annu. Rev. Fluid Mech.* 30 (1998) 139–165.
- [17] J. Kim, Phase-field models for multi-component fluid flows, *Commun. Comput. Phys.* 12 (3) (2012) 613–661.
- [18] T. Mitchell, C. Leonardi, A. Fakhari, Development of a three-dimensional phase-field lattice Boltzmann method for the study of immiscible fluids at high density ratios, *Int. J. Multiph. Flow.* 107 (2018) 1–15.
- [19] S. Aihara, T. Takaki, N. Takada, Multi-phase-field modeling using a conservative Allen–Cahn equation for multiphase flow, *Comput. & Fluids* 178 (15) (2019) 141–151.
- [20] Y.Q. Zu, S. He, Phase-field-based lattice Boltzmann model for incompressible binary fluid systems with density and viscosity contrasts, *Phys. Rev. E* 87 (2013) 043301.
- [21] F. Ren, B. Song, M.C. Sukop, H. Hu, Improved lattice Boltzmann modeling of binary flow based on the conservative Allen–Cahn equation, *Phys. Rev. E* 94 (2016) 023311.
- [22] A. Fakhari, T. Mitchell, C. Leonardi, D. Bolster, Improved locality of the phase-field lattice–Boltzmann model for immiscible fluids at high density ratios, *Phys. Rev. E* 96 (2017) 053301.
- [23] R.H.H. Abadi, M.H. Rahimian, A. Fakhari, Conservative phase-field lattice–Boltzmann model for ternary fluids, *J. Comput. Phys.* 374 (2018) 668–691.
- [24] M. Lepilliez, E.R. Popescu, F. Gibou, S. Tanguy, On two-phase flow solvers in irregular domains with contact line, *J. Comput. Phys.* 321 (2016) 1217–1251.
- [25] Y.T. Ng, C. Min, F. Gibou, An efficient fluid–solid coupling algorithm for single-phase flows, *J. Comput. Phys.* 228 (2009) 8807–8829.
- [26] H. Zolfaghari, D. Izbassarov, M. Muradoglu, Simulations of viscoelastic two-phase flows in complex geometries, *Comput. & Fluids* 156 (2017) 548–561.
- [27] H. Liu, K. Mu, H. Dong, Simulation of incompressible multiphase flows with complex geometry using etching multiblock method, *Appl. Math. Model.* 37 (11) (2016) 1405–1418.
- [28] Y. Li, D. Jeong, J. Shin, J. Kim, A conservative numerical method for the Cahn–Hilliard equation with Dirichlet boundary conditions in complex domains, *Comput. Math. Appl.* 65 (2013) 102–115.
- [29] A. Fakhari, D. Bolster, Diffuse interface modeling of three-phase contact line dynamics on curved boundaries: A lattice Boltzmann model for large density and viscosity ratios, *J. Comput. Phys.* 334 (2017) 620–630.
- [30] D. Jeong, J. Yang, J. Kim, A practical and efficient numerical method for the Cahn–Hilliard equation in complex domains, *Commun. Nonlinear Sci. Numer. Simul.* 73 (2019) 217–228.

- [31] X. Yang, J. Zhao, Q. Wang, J. Shen, Numerical approximations for a three-component Cahn–Hilliard phase-field model based on the invariant energy quadratization method, *Math. Models Methods Appl. Sci.* 27 (2017) 1993–2030.
- [32] Y. Cai, H. Choi, J. Shen, Error estimates for time discretizations of Cahn–Hilliard and Allen–Cahn phase-field models for two-phase incompressible flows, *Numer. Math.* 137 (2017) 417–449.
- [33] C. Xu, T. Tang, Stability analysis of large time-stepping methods for epitaxial growth models, *SIAM J. Numer. Anal.* 44 (2005) 1759–1779.
- [34] H. Garcke, B. Nestler, B. Stoth, On anisotropic order parameter models for multiphase systems and their sharp interface limits, *Physica D* 115 (1998) 87–108.
- [35] H.G. Lee, J. Kim, A second-order accurate non-linear difference scheme for the N-component Cahn–Hilliard system, *Physica A* 387 (2008) 19–20.
- [36] J. Kim, A continuous surface tension force formulation for diffuse-interface models, *J. Comput. Phys.* 204 (2005) 784–804.
- [37] H.G. Lee, J. Kim, Two-dimensional Kelvin–Helmholtz instabilities of multi-component fluids, *Eur. J. Mech. B Fluids* 49 (2015) 77–88.
- [38] T. Young, An essay on the cohesion of fluids, *Philos. Trans. R. Soc. Lond.* 95 (1805) 65–87.
- [39] H. Ding, P.D.M. Spelt, Wetting condition in diffuse interface simulations of contact line motion, *Phys. Rev. E* 75 (2007) 046708.
- [40] Y. Li, J. Choi, J. Kim, Multi-component Cahn–Hilliard system with different boundary conditions in complex domains, *J. Comput. Phys.* 323 (2016) 1–16.
- [41] U. Trottenberg, C. Oosterlee, A. Schuller, *Multigrid*, Academic Press, 2000.
- [42] J. Kim, K. Kang, J. Lowengrub, Conservative multigrid methods for Cahn–Hilliard fluids, *J. Comput. Phys.* 193 (2004) 511–543.
- [43] A.J. Chorin, A numerical method for solving incompressible viscous flow problems, *J. Comput. Phys.* 2 (1967) 12–26.
- [44] F.H. Harlow, J.E. Welch, Numerical calculation of time-dependent viscous incompressible flow of fluid with free surface, *Phys. Fluids* 8 (1965) 2182–2189.
- [45] J.W. Choi, H.G. Lee, D. Jeong, J. Kim, An unconditionally gradient stable numerical method for solving the Allen–Cahn equation, *Physica A* 338 (9) (2009) 1791–1803.
- [46] Y. Li, E. Jung, W. Lee, H.G. Lee, J. Kim, Volume preserving immersed boundary methods for two-phase fluid flows, *Internat. J. Numer. Methods Fluids* 69 (2012) 842–858.
- [47] H. Ding, P.D.M. Spelt, C. Shu, Diffuse interface model for incompressible two-phase flows with large density ratios, *J. Comput. Phys.* 226 (2007) 2078–2095.
- [48] Q. Li, K.H. Luo, Y.J. Gao, Y.L. He, Additional interfacial force in lattice Boltzmann models for incompressible multiphase flows, *Phys. Rev. E* 85 (2012) 026704.
- [49] J.L. Guermond, L. Quartapelle, A projection FEM for variable density incompressible flows, *J. Comput. Phys.* 165 (2000) 167–188.
- [50] R. Chen, X. Yang, H. Zhang, Decoupled, energy stable scheme for hydrodynamic Allen–Cahn phase field moving contact line model, *J. Comput. Math.* (2018) <http://dx.doi.org/10.4208/jcm.1703-m2016-0614>.